Inorg. Chem. **2007**, *46*, 10200–10207

Inorganic Chemistry Article

Adaptable Thermochromism in the $CuMo_{1-x}W_xO_4$ Series ($0 \leq x < 0.1$): A Behavior Related to a First-Order Phase Transition with a Transition Temperature Depending on x

M. Gaudon,*,[†] C. Carbonera,[†] A. E. Thiry,[‡] A. Demourgues,[†] P. Deniard,[‡] C. Payen,[‡] J.-F. Létard,[†] and S. Jobic[‡]

Institut de Chimie de la Matière Condensée de Bordeaux, UPR 9048 CNRS, 87 Avenue du Docteur Schweitzer, 33608 PESSAC Cedex, France; Institut des Matériaux Jean Rouxel (I.M.N), UMR 6502 CNRS, Université de Nantes, Nantes Atlantique Universités, 2 rue de la Houssinière, BP 32229, 44322 Nantes Cedex 3, France

Received June 27, 2007

The members of the $CuMo_{1-x}W_xO_4$ series ($0 \leq x < 0.1$) undergo a first-order phase transition at normal pressure, which can be induced by temperature. The two allotropic forms exhibit two distinguishable colors, green for the high-temperature form (α) and brownish-red for the low temperature one (γ), which opens up a new market for user-friendly temperature indicators. From X-ray diffraction and microprobe analyses as from optical properties, the tungsten substitution rate for molybdenum is limited to 12%. Beyond, a third, parasitic wolframite-type phase, $CuMo_{0.6}W_{0.4}O_6$, systematically crystallizes besides the $\alpha/\gamma CuMo_{0.9}W_{0.1}O_4$ compounds. Within the $CuMo_{1-x}W_xO_4$ solid-solution domain, the dependence of the transition temperatures was followed by calorimetry, optical reflectivity, and magnetism. On the basis of these measurements, the transition is characterized for all of the chemical compositions by a hysteresis loop of about 90 K in width with a temperature transition strongly dependent on the tungsten content. Namely, the $\gamma \rightarrow \alpha$ transition can occur between 260 and 360 K, and the $\alpha \rightarrow \gamma$ transition between 175 and 275 K as a function of x. The control of the α/γ transition temperatures with x is related to the larger propensity of tungsten compared to molybdenum, to adopt a tetrahedral environment.

1. Introduction

Currently, thermochromic materials receive much attention due to their potential applications as user-friendly temperature indicators in a wide range of devices such as chill checkers, cooking tools, hotplates, medical strips, sterilization displays, fridges, furnaces... Generally speaking, thermochromic materials can be defined as materials presenting a reversible or irreversible change in color, with respect to temperature.[1] Practically, organic compounds or liquid crystals are used for applications at temperatures lower than about 400 K. For higher temperatures, this kind of material may deteriorate due to their intrinsic, low thermal stability.

Then, inorganic materials may be of great interest as substitutes because of their higher stability and durability upon temperature cycling.

For oxides, various mechanisms may be at the origin of the color change with temperature increase: continuous reduction of the band gap for semiconducting oxides leading to a red shift,[2−4] reduction of the ligand field on a chromophore cation due to thermal dilatation as in chromium-doped Al_2O_3 ruby,[2] or phase transition implying a change in electronic transition energies and/or insulating/metallic behavior transitions as for VO_2 oxide,[5−12] $BaMnO_3$,[13] or

---

* To whom correspondence should be addressed: Email: gaudon@icmcb-bordeaux.cnrs.fr, Fax: (33)05.40.00.66.34.

[†] Institut de Chimie de la Matière Condensée de Bordeaux.

[‡] Université de Nantes.

(1) Day, J. H. *Chem. Rev.* **1968**, *68*, 6.

(2) Nassau, K. *The Physics and Chemistry of Color*; Published by John Wiley and Sons Inc., 1983u.

(3) Eom, S. H.; Kim, D. J.; Yu, Y.-M.; Choi, Y. D. *J. Alloys Compd.* **2005**, *388* (2), 190.

(4) Askenov, N.; Schubert, M.; Czakai, W.; Benndorf, G.; Hochmuth, H.; Lorenz, M.; Grundmann, M. *Phys. Rev. B* in press.

(5) Lee, M.-H.; Kim, M.-G. *Thin Solid Films* **1996**, *286* (1−2), 219.

(6) Jin, P.; Nakao, S.; Tanemura, S. *Nucl. Instrum. Methods Phys. Res., Sect. B* **1998**, *141* (1−4), 419.

(7) Nunes, G. G.; Friedermann, G. R.; dos Santos, J. L. B.; Herbst, M. H.; Vugman, N. V.; Hitchcock, P. B.; Leigh, G. J.; Sá, E. L.; da Cunha, C. J.; Soares, J. F. *Inorg. Chem. Commun.* **2005**, *8* (1), 83.

(8) Sobhan, M. A.; Kivaisi, R. T.; Stjerna, B.; Granqvist, C. G. *Sol. Energy Mater. Sol. Cells* **1996**, *44* (4), 451.

(9) Xu, G.; Jin, P.; Tazawa, M.; Yoshimura, K. *Sol. Energy Mater. Sol. Cells* **2004**, *83* (1), 29.

10.1021/ic701263c CCC: $37.00

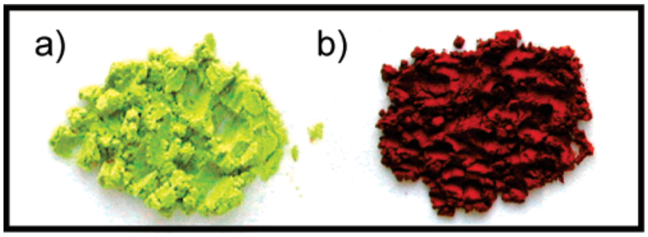

Figure 1. Colors of α-CuMo$_{0.925}$W$_{0.075}$O$_4$ in the high-temperature form (a) and γ-CuMo$_{0.925}$W$_{0.075}$O$_4$ in the low-temperature form (b) with $L = 72.2$, $a = -7.9$ and $b = 52.0$, and $L = 46.7$, $a = 14.9$ and $b = 22.9$, respectively.

MoO$_3$.[14] The advantage of the latter category of materials is that the materials that exhibit a phase transition are the only ones associated with a drastic change in color at a desired temperature. Indeed, reductions in the band gap in semiconductors and reductions of ligand field energy with dilatation are soft and progressive phenomena.

Recently, the temperature dependence of the optical properties of CuMoO$_4$ were reported by G. Steiner et al.,[15] the pressure dependence on the absorption spectrum of CuMoO$_4$ by D. Hernández et al.,[16] whereas the unprecedented "one finger push" induced-phase transition in the CuMo$_{0.9}$W$_{0.1}$O$_4$ compound was discussed by M. Gaudon et al.[17] Indeed, the CuMo$_{1-x}$W$_x$O$_4$ oxides ($0 \leq x < 0.1$) appear as materials of interest for thermochromic applications because they exhibit, at normal pressure, two distinct allotropic forms already described in the literature for CuMoO$_4$.[18−20] The high-temperature (low-pressure) α form is green, whereas the low-temperature (high-pressure) γ form is brownish-red as depicted in Figure 1 for CuMo$_{0.925}$W$_{0.075}$O$_4$. Versus the tungsten content, these first-order $\gamma \rightarrow \alpha$ and the $\alpha \rightarrow \gamma$ transitions may occur between 260 K and 360K, and between 175 and 275 K upon heating and cooling, respectively, with a hysteresis loop of about 85 K in width.[17]

In this article, the solubility limit of tungsten in CuMo$_{1-x}$W$_x$O$_4$ oxide is probed whereas the influence of the tungsten content on the thermochromic properties are characterized and discussed. The stabilization at room temperature of pure α-type samples upon cooling after synthesis at 700 °C has allowed an optical characterization by reflectivity measurements in the UV-vis region, and a new interpretation of the spectra is given. Moreover, the transition temperature modifications with tungsten substitution are carefully analyzed via three different techniques, calorimetry, reflectivity, and magnetism, and interpreted with respect to a first-order transition thermodynamic model. As reported in ref 19, the ternary CuMo$_{1-x}$W$_x$O$_4$ oxides also exhibit irreversible piezochromic/tribochromic properties. These properties will be detailed elsewhere. Hereafter, the synthesis and the investigation techniques are summarized in section 2. In section 3, after a brief description of the structural types, we discuss the solubility limit of tungsten in CuMo$_{1-x}$W$_x$O$_4$, the optical properties, and the temperature of the $\alpha \leftrightarrow \gamma$ transition determined via temperature-dependent reflectivity, differential scanning calorimetry (DSC), and magnetic measurements. Finally, essential findings of our work are summarized at the end of the discussion section.

2. Experimental Section

Synthesis. CuMo$_{1-x}$W$_x$O$_4$ polycrystalline samples were prepared through solid-state reactions. Briefly, the constituent oxides Cu$_2$O (Alfa-Aesar, 99%), MoO$_3$ (Alfa-Aesar, 99.95%), and WO$_3$ (Fluka, 99.9%) were intimately mixed in the prerequisite proportions, in an agate mortar. Then, the mixture was ball-milled in an agate container partially filed with acetone. The blend was calcined at 700 °C for 24 h and cooled down to room temperature.

Powder X-ray Diffraction. Powder X-ray diffraction patterns were recorded in a Debye−Scherrer geometry on an INEL diffractometer equipped with a 120° Curved Position Sensitive Detector with monochromatic Cu $K\alpha$ radiation (1.540598 Å) and with a spatial resolution of 0.03°. Data were collected over the 5−120° 2θ range for at least 12 h. The structure refinements of the triclinic α and γ forms were carried out via a Rietveld analysis by means of the *FullProf* package

Microprobe Analysis. Elemental composition was determined by means of a Castaing microprobe CECAMA SX 630 apparatus by wavelength dispersive spectrometry. Analyses were performed on uniaxial pressed-powdered pellets and yield the relative copper/molybdenum/tungsten molar ratios. The oxygen content was deduced to ensure the right charge balance, the oxidation states of copper, molybdenum, and tungsten being taken to be equal to II, VI, and VI, respectively. Each microprobe analysis was repeated three times in three distinct zones. Error bars on each composition measurement were calculated from the standard deviation and tend to be less than 1 mol %. Furthermore, it has to be specified that the analyses were performed with a probe volume size of 1 μm^3, that is, for a volume significantly lower than that of each probed particle of the pellets.

DSC Measurements. The differential scanning calorimetry (DSC) analyses were made on a PerkinElmer DSC7 calorimeter with charge compensation. The data were collected with a heating and cooling rate of 10 K·min^{-1} in the 50−400 K temperature range. The apparatus characteristics were recorded just before the samples' measurements, using the same thermal cycles for posterior subtractions.

Magnetic Susceptibility Measurements. Magnetic measurements were done on the superconducting quantum interference device (SQUID) apparatus Cryogenix S600 magnetometer within the temperature range of 5−340 K at atmospheric pressure. All of the measurements were performed with heating and cooling rates

---

(10) Sobhan, M. A.; Kivaisi, R. T.; Stjerna, B.; Granqvist, C. G. *Sol. Energy Mater. Sol. Cells* **1996**, *44* (4), 451.
(11) Jin, P.; Tanemura, S. *Thin Solid Films* **1996**, *239*, 281−282.
(12) Livage, J. *Coord. Chem. Rev.* **1999**, *391*, 190−192.
(13) Heiras, J.; Pichardo, E.; Mahmood, A.; López, T.; Pérez-Salas, R.; Siqueiros, J. M.; Castellanos, M. *J. Phys. Chem. Solids* **2002**, *63* (4), 591.
(14) Quevedo-Lopez, M. A.; Ramirez-Bon, R.; Orozco-Teran, R. A.; Mendoza-Gonzalez, O.; Zelaya-Angel, O. *Thin Solid Films* **1999**, *202*, 343−344.
(15) Steiner, G.; Salzer, R.; Reichelt, W.; Fresenius, J. *Anal. Chem.* **2001**, *370*, 731−734.
(16) Hernández, D.; Rodrìguez, F.; Garcia-Jaca, J.; Ehrenberg, H.; Weitzel, H. *Physica B* **1999**, *265*, 181−185.
(17) Gaudon, M.; Jobic, S.; Demourgues, A.; Deniard, P.; Thiry, A-E.; Carbonera, C.; Le Nestour, A.; Largeteau, A.; Létard, J.-F. submitted, 2007.
(18) Hernández, D.; Rodríguez, F.; Garcia-Jaca, J.; Ehrenberg, H.; Weitzel, H. *Physica B* **1999**, *265* (1−4), 181.
(19) Wiesmann, M.; Ehrenberg, H.; Miehe, G.; Peun, T.; Weitzel, H.; Fuess, H. *J. Solid State Chem.* **1997**, *132* (1), 88.
(20) Ehrenberg, H.; Weitzel, H.; Paulus, H.; Wiesmann, M.; Wltschek, G.; Geselle, M.; Fuess, H. *J. Phys. Chem. Solids* **1997**, *58* (1), 153.

of 10 K·min^{-1}. The data were corrected for the magnetic signal of the sample holder and for diamagnetic contributions of the constituents estimated from Pascal's constants.

Reflectivity Measurements. Room-temperature UV−vis-NIR diffuse reflectance spectra were collected on a finely ground sample with a Cary 17 spectrometer (Varian) equipped with a 60 mm diameter integrating sphere. Diffuse reflectance was measured from 200 to 1500 nm using Halon powder (from Varian) as a reference (100% reflectance). 1964-CIE Lab system parameters were determined by a mathematical conversion of the reflectivity signal treatment. Low-temperature reflectance was collected on powder via two home-built instruments, that is, a setup equipped with a CVI spectrometer, which allows us to follow the evolution of UV-vis spectra in the 400 to 900 nm range between 5 and 290 K and a setup equipped with a photomultiplicator to collect, in the 150−395 K temperature range, the integrated reflected intensity of a green-filtered white-light incident beam (500−550 nm). In both cases, the white-light source was a halogen lamp, and the heating/cooling rate was settled at 10 K·min^{-1}.

3. Results and Discussion

Brief Structural Description of α and γ-$CuMo_{1-x}W_xO_4$ Phases. All of the members of the $CuMo_{1-x}W_xO_4$ series ($x \leq 0.12$) may crystallize in the α-$CuMoO_4$ and γ-$CuMoO_4$ structure types with $P\bar{1}$ as a space group.[18−21] In the α form, $^1/_3$ and $^2/_3$ of Cu^{2+} cations occupied [CuO_5] square-pyramids and [CuO_6] elongated octahedra, respectively, whereas Mo^{6+} or W^{6+} cations sit at the center of a [MoO_4] tetrahedral site. In the γ form, all of the Cu^{2+} and Mo^{6+} (and W^{6+}) ions display an octahedral coordination. The α → γ transition goes along with a ~12% shrinkage of the cell volume, whatever the tungsten concentration, for example, a = 9.8989(2) Å, b = 6.7931(1) Å, c = 8.3569(2) Å, α = 101.154(2)°, β= 96.902(1)°, γ = 107.38(1)°, and V = ~5198 Å^3, and a = 9.7175(3) Å, b = 6.3100(2) Å, c = 7.9786(3) Å, α = 94.727(4)°, β = 103.345(3)°, γ = 103.318(3)°, V = ~458 Å^3 for α-$CuMo_{0.90}W_{0.1}O_4$ and γ-$CuMo_{0.90}W_{0.1}O_4$, respectively.

Solubility Limit of Tungsten in $CuMo_{1-x}W_xO_4$. The purity and the exact chemical composition of $CuMo_{1-x}W_xO_4$ compounds with $0 \leq x \leq 0.5$ were investigated by X-ray diffraction and microprobe analysis. First, the X-ray patterns clearly evidence that for low tungsten content ($x < 0.12$), all of the diffraction peaks obtained can be indexed as belonging to α-$CuMo_{1-x}WxO_4$ or γ-$CuMo_{1-x}WxO_4$ triclinic phases (Figure 2). However, for high tungsten content ($x > 0.12$), a third phase is detected, which crystallizes in the wolframite-type structure as $CuWO_4$. To support this segregation for a high tungsten rate, Figure 2 displays the X-ray diffraction patterns obtained on the $CuMo_{0.9}W_{0.1}O_4$ composition, for which a mixture of α and γ forms is obtained and for the $CuMo_{0.7}W_{0.3}O_4$ nominal composition, for which a mixture of the three phases (α, γ, and wolframite-type forms) is obtained. Second, the microprobe analyses were carried out to determine exact chemical composition of the bistable composition composed of α and γ forms (hereafter noted boron composition) and wolframite-type phase (hereafter noted tungsten phase) versus the tungsten amount in the target composition.

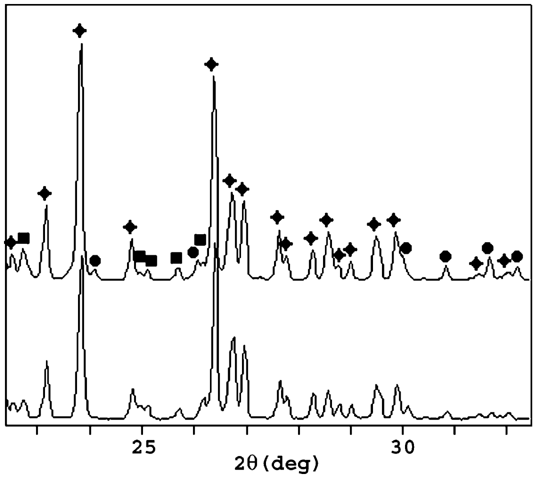

Figure 2. X-ray Diffraction patterns of the phase mixture for $CuMo_{0.9}W_{0.1}O_4$ (a) and $CuMo_{0.7}W_{0.3}O_4$ (b) nominal compositions. ((♦) α-CuMoO4 structure type, (■) γ−$CuMoO_4$ structure type, (●) wolframite structure type).

As illustrated on the electronic density micrographs reported in the Figure 3, when the tungsten phase is present, it can be easily detected. Indeed, this latter phase, which contains the largest tungsten rate and thus the highest electronic density, appears white, whereas the boron composition with lower tungsten content appears gray; at least the pellet porosity appears black.

It was possible to limit the probed volume to a zone inferior than the particle size (gray or white areas). Hence, for each sample, the chemical composition of boron and tungsten can be extracted. In Table 1 is a sum-up of the elemental analyses of $CuMo_{1-x}W_xO_4$ samples with x ranging from 0 to 0.5. First, from these results, the solubility limit in tungsten in the $CuMo_{1-x}W_xO_4$ α/γ structure type is clearly between 0.1 and 0.15. Indeed, for $x \leq 0.1$, only the boron composition is detected, whereas for $x > 0.15$, the presence of the tungsten phase is clearly identified. This observation appears to be in agreement with X-ray diffraction investigations, which only evidence α and γ structure types. One can notice that, the boron composition presents a small molybdenum or tungsten deficiency depending on the sample, in comparison with the target compositions, a phenomenon probably caused by raw material impurities and/or their slight hydratation, leading to slight weighing errors. Moreover, the microprobe analyses indicate that the chemical composition of boron and tungsten does not change for nominal $CuMo_{1-x}W_xO_4$ chemical composition, with x higher than the solubility limit. This phenomenon is clearly associated with the existence of a miscibility gap between the boron and tungsten phases. The compositions of the two extremes of the boron and tungsten solid solutions on both sides of the miscibility gap could be estimated as about $CuMo_{0.88}W_{0.12}O_4$ and $CuMo_{0.4}W_{0.6}O_4$, respectively. More-detailed analyses made on the electronic density micrographs have confirmed that the total tungsten rate of the sample does not influence the two final compositions but, in fact, controls their volume ratio. Indeed, this behavior could be characterized by image treatment, using *ImageTool* software, of the electronic density micrographs. As illustrated on the

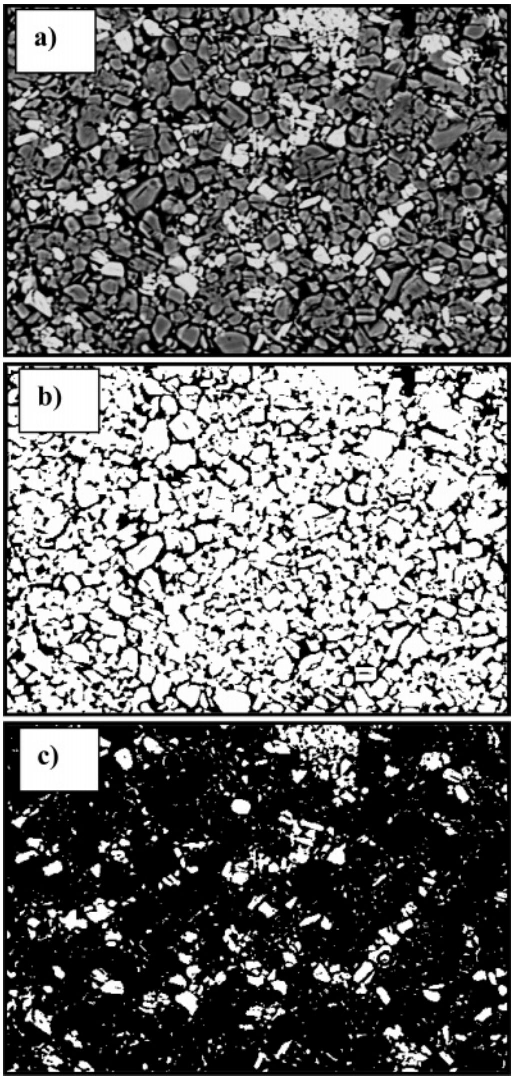

Figure 3. Electronic density micrograph (a) and binary pictures obtained after image thresholds 1 (b) and 2 (c), respectively. Gray and white grains are assigned to the boron composition and the tungsten phase, black spots to porosity. Micrographs represent a 150 × 250 μm^2 area.

Figure 3, the phases volume ratio can be obtained, proceeding by a double binarization of the numeric micrographs, putting in evidence of the total-solid volume (threshold 1) and the tungsten-phase volume (threshold 2). Finally, an integration of white and blacks areas obtained after each binarization is performed for volume quantifications. Elsewhere, considering in a first approximation that the molar ratio between the wolframite and triclinic phases is equal to their volume ratio, an overall composition can be calculated and compared to the target one. In all of the cases, a high proximity of the these compositions was observed that validates the existence of the gap of miscibility as well as the solubility limit values of tungsten in the boron composition and of molybdenum in the tungsten phase.

UV−Vis Properties at Room Temperature. At room temperature, reflectivity spectra have been recorded on α-$CuMo_{1-x}W_xO_4$ compounds, for which their tungsten rate allows the stabilization of a pure single α-phase in ambient conditions, that is, for $x \leq 0.075$. Indeed, for higher tungsten content, only a mixture of α and γ phases can be obtained due to the propensity of the α form to partially transit into the γ form. In Figure 4, the optical-absorption spectra (Kubelka Munk transformed: K/S curves) collected for three compositions, $x = 0$, 0.05, and 0.075, are reported to underline the influence of the substitution of molybdenum for tungsten on the α-form colorimetric parameters. CIE Lab parameters are given in Table 2.

Table 1. Elemental Analyses of $CuMo_{1-x}W_xO_4$ Samples Obtained by Castaing Microprobe

nominal composition	cationic proportion	analyzed compositions
$CuMo_{0.98}W_{0.02}O_4$	**B composition** Cu/(Mo + W) = 1.03 W/(Mo + W) = 0.02	$CuMo_{0.98}W_{0.02}O_4$
$CuMo_{0.95}W_{0.05}O_4$	**B composition** Cu/(Mo + W) = 1.03 W/(Mo + W) = 0.06	$CuMo_{0.94}W_{0.06}O_4$
$CuMo_{0.90}W_{0.10}O_4$	**B composition** Cu/(Mo + W) = 1.03 W/(Mo + W) = 0.10	$CuMo_{0.90}W_{0.10}O_4$
$CuMo_{0.85}W_{0.15}O_4$	**B composition** Cu/(Mo + W) = 1.02 W/(Mo + W) = 0.12	$CuMo_{0.88}W_{0.12}O_4$
	W phase Cu/(Mo + W) = 1.01 W/(Mo + W) = 0.59	$CuMo_{0.41}W_{0.59}O_4$
$CuMo_{0.80}W_{0.20}O_4$	**B composition** Cu/(Mo + W) = 1.02 W/(Mo + W) = 0.11	$CuMo_{0.89}W_{0.11}O_4$
	W phase Cu/(Mo + W) = 1.01 W/(Mo + W) = 0.60	$CuMo_{0.40}W_{0.60}O_4$
$CuMo_{0.70}W_{0.30}O_4$	**B composition** Cu/(Mo + W) = 0.94 W/(Mo + W) = 0.10	$CuMo_{0.90}W_{0.10}O_4$
	W phase Cu/(Mo + W) = 1.00 W/(Mo + W) = 0.58	$CuMo_{0.42}W_{0.58}O_4$
$CuMo_{0.50}W_{0.50}O_4$	**B composition** Cu/(Mo + W) = 0.93 W/(Mo + W) = 0.10	$CuMo_{0.90}W_{0.10}O_4$
	W phase Cu/(Mo + W) = 0.96 W/(Mo + W) = 0.61	$CuMo_{0.39}W_{0.61}O_4$

The general feature of the K/S curves of the three materials is very similar. For all of the compositions, the optical spectrum evidenced two absorption bands, one located below ∼1.8 and one located above ∼2.5 eV, in good agreement with the observed green color of the material. The former is commonly associated with Cu^{2+} d−d transitions, whereas

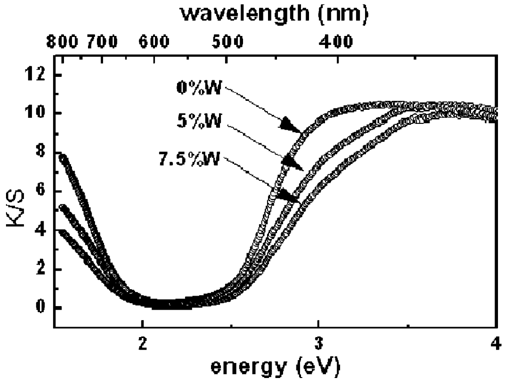

Figure 4. Room-temperature Kubelka−Munk spectra of $CuMoO_4$, $CuMo_{0.95}W_{0.05}O_4$, and $CuMo_{0.925}W_{0.075}O_4$ oxides in their α form.

Table 2. CIE Lab Parameter of α-$CuMo_{1-x}W_xO_4$ Oxides at Room Temperature ($x = 0$, 0.05, and 0.075)

compounds formula	optical parameters $L - a - b$
$CuMoO_4$	69.6 − 6.9 − 57.0
$CuMo_{0.95}W_{0.05}O_4$	72.3 − 8.2 − 53.8
$CuMo_{0.925}W_{0.075}O_4$	77.7 − 10.0 − 55.7

the latter would be due, according to Hernǎndez et al.[18] and Rodríguez et al.,[21] to an $O^{2-} \rightarrow Cu^{2+}$ charge transfer (CT). At this stage, this last assignment is somewhat questionable, and we wonder whether an $O^{2-} \rightarrow Mo^{6+}$, W^{6+} CT assignment would be not preferable, to account for the high-energy absorption for the following reasons: (i) a regular increase of the $O^{2-} \rightarrow Mo^{6+}$, W^{6+} CT is expected with tungsten concentration[22] as observed in Figure 4. At the opposite, the $O^{2-} \rightarrow Cu^{2+}$ CT should remain almost unmodified for a substitution rate as low as 5% because the copper environment is not directly perturbed, (ii) another ternary oxide: $ZnMoO_4$ with the same α-form triclinic structure presents a $O^{2-} \rightarrow Mo^{6+}$ CT more or less at the same position in energy (iii) Furthermore, it will be shown that the thermochromism is linked to this CT shift, and a comparative thermochromism effect is observed for the ternary oxide $CoMoO_4$, where a phase transition involving a change in the molybdenum coordination also occurs. Consequently, it appears quite seductive to associate the color change going from α-$CuMoO_4$ to γ-$CuMoO_4$ to a change in molybdenum coordination from tetrahedral to octahedral. Whatever may be the case, that means the CT between the oxygen and the first empty molybdenum 4d orbital appears at an energy energy lower than that of the CT from the oxygen first empty copper 3d orbital. Such a hypothesis could be well explained by two phenomena : (i) the d-orbital splitting due to the strong octahedral ligand field coupled with a Jahn−Teller effect on Cu^{2+} ($4s^0 3d^9$), and (ii) the CT from ligand to Cu^{2+} ($3d^9$) implies that the electron transfer takes place in a half occupied orbital, what implies the creation of an intrasite columbic repulsion contribution. Whatever may be the case, from the spectral curves reported in Figure 4, which evidence an enhancement of the reflectivity window versus the molybdenum/tungsten substitution, it appears, as summed up in Table 2, that α-$CuMo_{1-x}W_xO_4$ oxides exhibit a luminosity L, which increases with x, whereas the a and b colorimetric parameters remain almost constant, probably because the center of the reflectivity window does not move in energy with x. Nevertheless, the green coloration is more and more dirtlike (the green transforms into an olive coloration) versus x, which is traduced by the slight increase of the a* colorimetric parameter.

UV−Vis Properties During the Phase Transition. Kubelka−Munk absortivity curves of $CuMoO_4$ between 30 and 280 K, are reported in Figure 5. First, upon cooling from room temperature to 185 K, a displacement of the absorption threshold associated with the $O^{2-} \rightarrow Mo^{6+}$ CT (vide supra) toward higher energy is observed. This is the expected trend for any semiconductor, and this phenomenon originates from the contraction of the α-$CuMoO_4$ cell parameters and a decrease of the oxygen−cation interatomic distances, which favors a stronger localization of the bond electrons around the ligand, and so, induce a higher energy to transfer the electron from the ligand top metal center. This goes along with a weak broadening of the reflectivity window, the positioning of the absorption band assigned to d−d transition being almost not affected by temperature, the crystal field being just a bit sensitive to temperature in comparison with CT. This trend agrees with the evolution of the transmission spectra of an α-$CuMoO_4$ crystal reported by Steiner et al.[15] in the 296−673 K temperature range. Second, between 200 and 10 K, the apparition of the γ-$CuMoO_4$ form results in the appearance of a new charge-transfer band located at lower energy concomitantly with a slight enlargement of the copper d−d absorption band due to the structure change. Consequently, upon cooling, a significant narrowing of the reflectivity window is observed due to a blue shift and a red shift of the d−d and $O^{2-} \rightarrow Mo^{6+}$ absorption bands, respectively. In regard of the crystallographic structure of the α and γ forms, the phenomenon can be explained by the transition of the Mo^{6+}/W^{6+} cations from tetrahedral to octahedral sites. It is well-known that a red shift of the ligand−metal charge transfer occurs when metal coordination increases[2]; indeed, the metal coordination increase is the cause of two phenomena linked to each other: the increase of the ligand coordination number (decrease of the effective charge directed toward each metallic metal center) and the increase of ligand−metal bond distances. Structural characterization has shown, besides the oxygen environment, that the phase transition leads to nearly no change in terms of the number of copper neighboring oxygens (from 17/18 in α to 1 in γ per oxygen) and Cu−O bond distances, whereas the number of molybdenum neighboring oxygens decreases (from 1.5 to 1 per oxygen) and Mo−O average distances increase. Consequently, Cu−O bonds appear quite stable between the two α and γ forms, whereas the average Mo−O bonds are

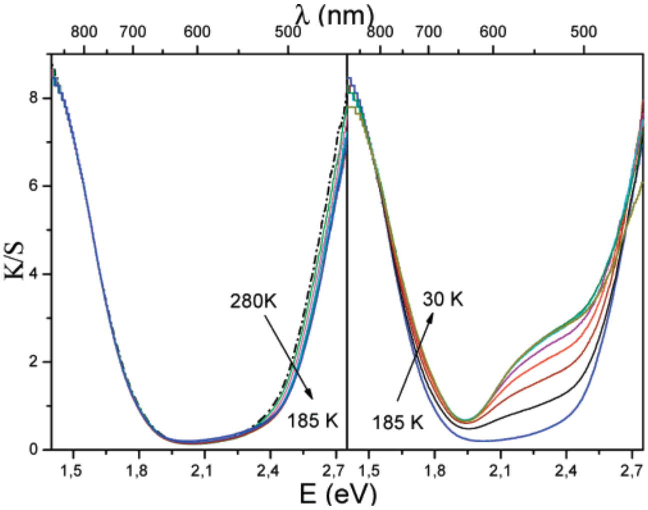

Figure 5. Evolution of Kubelka−Munk spectra of $CuMoO_4$ versus temperature.

---

(21) Rodríguez, F.; Hernandez, D.; Garcia-Jaca, J.; Ehrenberg, H.; Weitzel, H. *Phys. Rev. B* **2000**, *61*, 16497.

(22) Goubin, F.; Guénée, L.; Deniard, P.; Koo, H.-J.; Whangbo, M.-H.; Montardi, Y.; Jobic, S. *J. Solid State Chem.* **2004**, *177*, 4528.

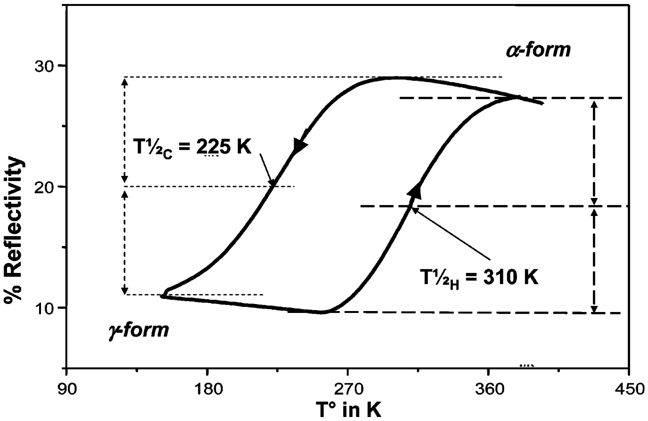

Figure 6. Evolution of the integrated reflectivity percentage in the green zone (500−550 nm) of $CuMo_{0.97}W_{0.03}O_4$ compound with temperature.

Table 3. $\alpha \rightarrow \gamma$ ($T_{1/2C}$) and $\gamma \rightarrow \alpha$ ($T_{1/2H}$) Temperature Transitions Issued from Reflectivity Measurements

compounds formula	$T_{1/2C}$ (K)	$T_{1/2H}$ (K)	$\Delta T_{1/2}$ (K)
Data extracted from the helium cooled setup			
$CuMoO_4$	175	247	72
$CuMo_{0.985}W_{0.015}O_4$	181	-	-
Data extracted from the nitrogen cooled setup			
$CuMo_{0.985}W_{0.015}O_4$	201	281	80
$CuMo_{0.97}W_{0.03}O_4$	222	310	78
$CuMo_{0.95}W_{0.05}O_4$	227	293	65
$CuMo_{0.925}W_{0.075}O_4$	251	352	101
$CuMo_{0.9}W_{0.1}O_4$	282	382	100

strongly modified by the phase transition; what underlines the thermochromism is well due to the Mo/W site modification and the high-energy absorption phenomenon is without any doubt $O^{2} \rightarrow Mo^{6+}/W^{6+}$ CT. Last, one can argue that the CT shift is a red shift one because the exchanged valence per bonds (bond effective charge) decreases from $^3/_2$ in α form to 1.0 in γ form. This effective charge decrease from α to γ form traduces, in a way, lower attraction of the bond electrons though the ligand side in *g* form, that is, it is a more probable possibility to transfer one electron from the ligand to the metal, that is, a low-energy absorption threshold.

α−γ Transition Temperatures Characterized by Reflectivity Measurement Versus *x*. The α ⇔ γ phase transition causes a drastic change in optical properties of the $CuMo_{1-x}W_xO_4$ solid solutions. In terms of absorption, the α form is very reflective in the green region, contrary to the γ form. Thus, the characterization of the phase transition can be initiated by means of reflectivity setup, allowing access to the integrated reflectivity in the 500−550 nm domain. Upon heating, the γ → α transition allows the determination of $T_{1/2H}$ temperature (corresponding, in a first approximation, to about 50 mol % of the α and γ phases). In the same way, the equivalent $T_{1/2C}$ temperature corresponding to the α → γ transition is recorded upon cooling. All of the members of the $CuMo_{1-x}W_xO_4$ series evidence a large hysteresis loop of the integrated reflected intensity versus temperature. The hysteresis width is hereafter characterized by the $\Delta T_{1/2} = T_{1/2C} - T_{1/2H}$. As an illustration, the evolution of the integrated reflectivity of the $CuMo_{0.97}W_{0.03}O_4$ oxide is displayed in Figure 6, where it schematized the procedure followed to extract the $T_{1/2C}$ and $T_{1/2H}$ temperatures. The relevant characteristics of the phase transition of $CuMoO_4$ and some of its tungsten-doped congeners are summed up in Table 3, the discrepancy for the two $CuMo_{0.985}W_{0.015}O_4$ datasets originating from the use of two different setups.

α−γ Transition Temperatures Characterized by DSC Measurements. In a first-order phase transition, the two involved forms get different reticular energy and total entropy, and the transition is accompanied by an enthalpy heat $\Delta H = T\Delta S$, with T = ideal to a first-order temperature of transition. Thus, by following the calorific capacity C_s of the sample with the temperature; the DSC process allows the calculation of the enthalpy heat ΔH with the equation:

$$dH/dt = dQ/dt + (C_s - C_{ref})dT/dt + RC_s d^2Q/dt^2$$

with Q = recorded power (watts), C_s and C_{ref} = calorific capacity of the sample and the apparatus, respectively ($J{\cdot}K^{-1}$), R = thermal resistance of the sample ($K{\cdot}W^{-1}$) and t = time (seconds).

The picture of part a of Figure 7 shows that normally two characteristic temperatures can be easily extracted by DSC measurements: The T_{onset}, which represents the ideal transition temperature, and the T_{peak} located at the signal maximum. Nevertheless, to extract the $T_{1/2}$ temperatures for direct comparison with the other characterization techniques, the integration of the peak was performed as shown in part b of Figure 7. Results are compiled in Table 4α−γ **Transition Temperatures Characterized by Magnetic Measurements.** Finally, another way to characterize the samples behavior versus the tungsten content is to perform magnetic measurements because of the presence of Cu^{2+} cations in the d^9

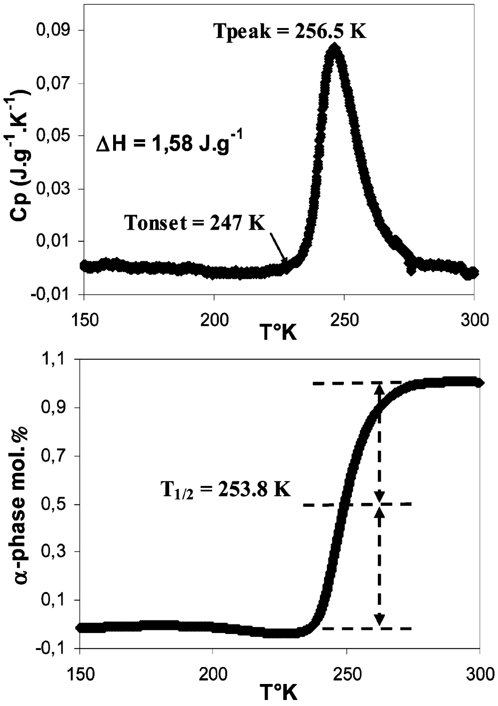

Figure 7. Heat-flow peak related to the γ → α transition with increasing temperature for the $CuMoO_4$ compound and integration of the collected signal.

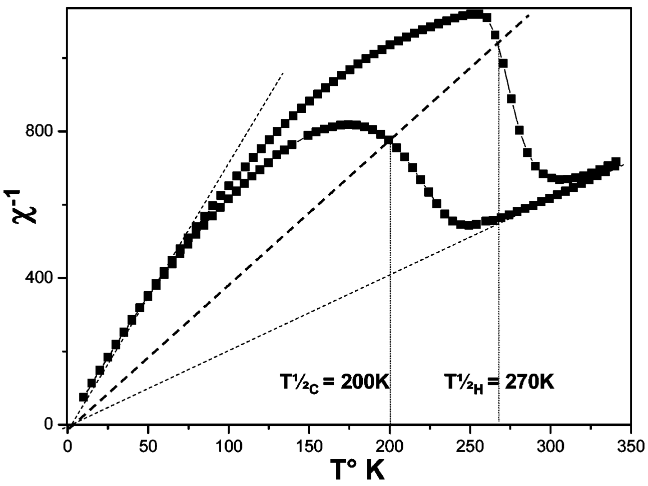

Figure 8. Evolution of the magnetic susceptibility of the $CuMo_{0.95}W_{0.05}O_4$ compound with the temperature.

Table 4. $\alpha \rightarrow \gamma$ ($T_{1/2C}$) and $\gamma \rightarrow \alpha$ ($T_{1/2H}$) Temperature Transitions Issued from DSC Measurements

compounds formula	$T_{1/2C}$ (K)	$T_{1/2H}$ (K)	$\Delta T_{1/2}$ (K)
$CuMoO_4$	158	254	96
$CuMo_{0.9}W_{0.1}O_4$	271	348	77

Table 5. $\alpha \rightarrow \gamma$ ($T_{1/2C}$) and $\gamma \rightarrow \alpha$ ($T_{1/2H}$) Temperature Transitions Issued from Magnetic Measurements

compounds formula	$T_{1/2C}$ (K)	$T_{1/2H}$ (K)	$\Delta T_{1/2}$ (K)
$CuMo\ O_4$	165	245	80
$CuMo_{0.95}W_{0.05}O_4$	202/223	273/284	73/61
$CuMo_{0.9}W_{0.1}O_4$	251/271.		65

electronic configuration, with a $S = {}^1/_2$ spin and a variable g factor function of the environment, leading to various susceptibilities. Because of the fact that the SQUID apparatus allows us to reach temperatures only up to 340 K, and only compounds with a doping fraction of up to $x = 0.05$ were susceptible to be studied. It should be noted here that the SQUID instrument allows a more-controlled speed in the temperature change with respect to the reflectivity apparatus. This analysis method was convenient because of the change of a part of the copper from a penta-coordinated insertion site to an octahedral site during the $\alpha-\gamma$ transition, leading to an evolution of the total g factor: $\mathrm{X} = N_A\beta/3kTg^2(S)(S + 1)$ with N_A = Avogadro number and k = Boltzman constant. Results obtained are reported in Table 5, and as an illustration, the magnetic loop recorded on $CuMo_{0.95}W_{0.05}O_4$ is plotted in Figure 8. Compared with reflected intensity change on cooling, the magnetic susceptibility evolves more gradually in the SQUID apparatus than in the reflectivity. This observation is probably due to kinetic effects, whereas the transition in the heating mode seems not to be affected from the kinetics, as well as from $T_{1/2}$ values, as it appears evident if we compare the values obtained on SQUID with the two other techniques.

To extract the $T_{1/2}$ temperatures, here, the bisector of the two $X^{-1} = f(T)$ linear curves is used as shown in picture 9, considering the susceptibility inverses are roughly additive. Results obtained with this last technique are reported in Table 5.

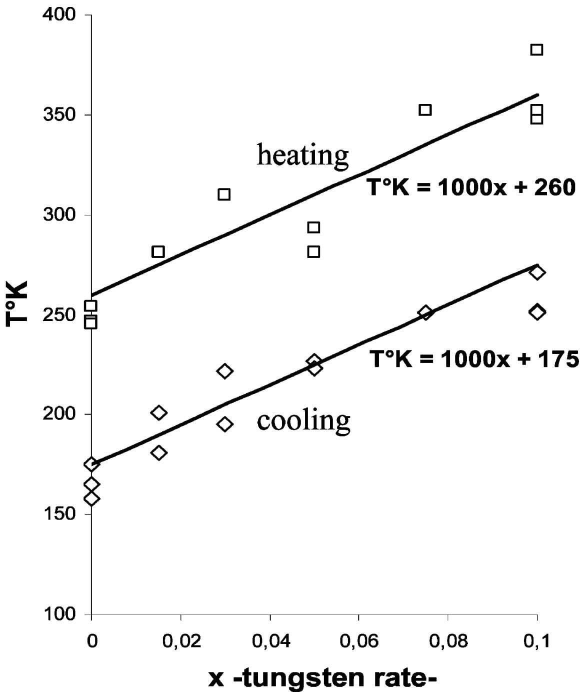

Figure 9. Evolution of the transition temperatures (during heating or cooling steps) plotted from the three techniques' results.

α-γ Transition. Conclusion. The difference between the $T_{1/2}$ values obtained from the different techniques can be considered resulting from uncertainties and artifacts inherent to measurement processes, and they will not be discussed here. The results obtained from the three techniques were put together; they are both reported in Figure 9. The aim of this study is not to conclude on respective advantages/disadvantages of each technique, but on the opposite, to combine three different techniques with different uncertainties and artifact sources to obtain a summation of all of the measurements to obtain a more-precise global trend for the transition temperatures' evolution versus the tungsten content.

Whatever may be the case, a significant increase in the temperature transition is observed when molybdenum is substituted for tungsten, in a parallel way for the heating and cooling mode. The evolution of $T_{1/2C}$ or $T_{1/2H}$ with the tungsten content x is roughly linear. Thus, these two evolutions were fitted as linear function. The two slopes are roughly similar, so the ΔT hysteresis between the cooling and heating temperatures can be considered as remaining constant with the tungsten content. Furthermore, this ΔT hysteresis can be approximated to 85 K. From the approximation made on the two curve slopes, it can be calculated that 10% of the tungsten substitution leads to an increase in the two transition temperatures of about 100 K. The outstanding point to underline is that this control of ±100 K on the transition temperatures allows for stabilizing of the α or the γ form around the room temperature. Briefly, we mention that the measured $T_{1/2}$ temperatures for the $CuMoO_4$ compound differ slightly from the values proposed by F. Rodriguez et al.[21] based on temperature dependence of a crystal optical density at 540 nm at ambient pressure with a cooling rate of 1 K/min (i.e., 10 times lower than here). The most important difference between the two studies resides in the hysteresis width; a $\Delta T_{1/2}$ of about only 20−30 K was proposed by Rodriguez. Such a large difference remains not easily explainable; it could be issued from two factors: Rodriguez worked with a lower heating/cooling rate, with a monocrystal.

The increase in the transition temperatures while tungsten is substituted for molybdenum can be explained in a first approximation by the stronger octahedra preference of W^{6+}, as compared to Mo^{6+}. It can be reminded as an illustration that $MgMoO_4$ crystallizes in the $C/2m$ crystallographic network where Mo^{6+} is 4-fold coordinated, whereas $MgWO_4$ crystallizes in the $P21/c$ network where W^{6+} is 6-fold coordinated. Tungsten will stabilize the octahedral site form, that is, the γ form to the detriment of the tetrahedral site form, that is, the α form. Furthermore, same considerations were made in the literature[11−12] to explain the control of the VO_2 phase transition temperatures where V^{4+} cations are substituted for Mo^{4+} or W^{4+}cations.

Finally, as an example, the $CuMo_{0.95}W_{0.05}O_4$ compound can be first stabilized at room temperature in its green-colored γ form by a preliminary cooling at a temperature below 225 K. This compound will then turn red (α form) at about 310 K, that is, human-body temperature. For this composition, the α form induced by a temperature of 310 K is still stable at room temperature because of the quite large ΔT hysteresis taking place on both sides of the room temperature. Hence, a slight variation of temperature and/or pressure will lead to a structural modification accompanied with a strong color variation. So, this material can be used as a convivial temperature as well as a pressure indicator. In a forthcoming article, the piezochromic properties of these $CuMo_{1-x}W_xO_4$ oxides will be discussed in more detail.

Acknowledgment. The authors wish to thank D. Denux, research engineer at the ICMCB, for DSC measurements.

IC701263C